

Article

SingMonitor: E-Bike Charging Health Monitoring Using Sound from Power Supplies

Xiangyong Jian, Lanqing Yang, Yijie Li, Yi-Chao Chen and Guangtao Xue *

School of Electronic Information and Electrical Engineering, Shanghai Jiao Tong University, Shanghai 200000, China; enhenf@sjtu.edu.cn (X.J.); yanglanqing@sjtu.edu.cn (L.Y.); yijieli@sjtu.edu.cn (Y.L.); yichao@utexas.edu (Y.-C.C.)

* Correspondence: xue-gt@cs.sjtu.edu.cn

Abstract: In recent years, fire disasters caused by charging electric bicycles/mopeds (e-bikes) have been increasing, causing catastrophic loss of life and property; Worse still, existing fire warning systems are costly to install and maintain, and they work after the accident occurs. Some existing works have proposed using power meters or similar sensors in the power grid to monitor e-bike charging health. However, the use of additional equipment makes them challenging to deploy. Others use the sound or electromagnetic signals emitted by e-bikes for monitoring; however, they suffer from limited monitoring distances. To solve this problem, we propose *SingMonitor*, a scheme to remotely monitor e-bike charging status using mobile device microphones. The charging e-bike generates a unique current signal, which is then transmitted through the power grid and drives the mobile devices' power supply to generate sound, which is then captured by a microphone. Based on this principle and the proposed template-matching method, *SingMonitor* can identify the e-bike charging status. Experiments show that *SingMonitor* achieved an F1 score of 0.94 in identifying 10 e-bike charging status, with a detection distance of 9 m+.

Keywords: e-bike; power supply; power factor correction; template matching



Citation: Jian, X.; Yang, L.; Li, Y.; Chen, Y.-C.; Xue, G. SingMonitor: E-Bike Charging Health Monitoring Using Sound from Power Supplies. *Appl. Sci.* **2023**, *1*, 0. <https://doi.org/>

Academic Editor: [Firstname Lastname](#)

Received: 3 December 2022

Revised: 13 February 2023

Accepted: 14 February 2023

Published:



Copyright: © 2023 by the authors. Licensee MDPI, Basel, Switzerland. This article is an open access article distributed under the terms and conditions of the Creative Commons Attribution (CC BY) license (<https://creativecommons.org/licenses/by/4.0/>).

1. Introduction

In recent years, electric bicycles/electric mopeds (here, both are referred to as “e-bikes”) have become increasingly popular, corresponding to the growing environmental awareness and technological advances in the e-bike industry, with the global e-bike market reaching 17.83 billion USD in 2021 [1]. Although e-bikes are convenient, they also generate certain safety threats. For example, there were nearly 18,000 fire disasters caused by charging e-bikes in China in 2021 [2].

Similarly, in October 2022, the USA recalled approximately 22,000 e-bikes whose lithium batteries could ignite, explode, or spark, posing fire, explosion, and burn hazards to consumers [3]. Low-quality batteries or chargers are some of the main reasons for these disasters [4,5]. In Section 3.1, we show how charger or battery quality issues can influence a battery’s capacity and even increase the risk of fire while charging. Worse yet, over time and with improper use (charging immediately after parking, etc.), even high-quality chargers and batteries can develop issues and become unreliable [6,7].

To prevent these disasters, many systems are dedicated to fire detection and alert, which can significantly reduce the damage caused by e-bike fires. For example, the Fire Alarm Control Unit (FACU) [8] is the mainstream commercial fire warning system. FACU consists of three parts: initiation devices (including various sensors and pull stations), the control panel, and sirens and fire-suppression devices. Refs. [9–15] focused on improving FACU systems with IoT technology. Such studies need to deploy many sensors or communication nodes with integrated sensors for rapid fire detection and alarm. They differ in the hardware and communication protocols used.

Refs. [16,17] analyzed data captured by closed-circuit television or webcams using image-processing technology to detect and track fires. However, these methods are costly to install and maintain and only work after a fire hazard occurs.

Some appliance detection methods can also monitor the charging health of e-bikes. For example, some of them use sensors to directly obtain the operating current, voltage, and load consumption of the appliances in the circuit [18–24]. Others use side-channel methods to identify appliances and their operating status by the electromagnetic [25,26] or acoustic signals [27,28] generated when the appliance is in operation. However, most of these methods require extra hardware, which makes them difficult for large-scale deployment, and some have limited monitoring distances.

Some battery-monitoring methods [29,30] use sensors to obtain information, such as the voltage and current of the battery to monitor the battery. Ref. [31] trained an LSTM model with voltage, temperature, and other information to monitor and protect the battery. Ref. [32] predicted the battery status through an electrochemical model. These methods require extra hardware devices to obtain information, such as the current and voltage, which increases the system's cost.

To solve this problem, in this paper, we propose *SingMonitor*—a scheme to remotely monitor e-bike charging health using mobile device microphones. *SingMonitor* can monitor the charger or battery for faults during daily charging, thereby, slowing battery capacity loss and, thus, preventing potential fire hazards. We created the *SingMonitor* system based on observations that:

(1) The charging e-bike can inject unique current signals into the power grid. Currently, e-bikes commonly use three-stage battery chargers [33]. At different charging stages, the power factor correction (PFC) circuit inside the e-bike charger can inject different feedback currents, i.e., PFC signals, into the power grid.

(2) The PFC signals can transmit through the power grid. As shown in Figure 1, PFC signals can be propagated along wires throughout the power grid. A detailed explanation can be found in Section 3.3.

(3) The PFC signals can drive the power supply at the other end of the grid to generate sounds. When the power supply of another appliance connected to the same distribution system receives this signal, it will emit a sound under electromagnetic forces.

(4) The sounds can be captured by nearby mobile devices and used to monitor the e-bike's charging health. By analyzing this sound signal, *SingMonitor* can obtain the current charging stage of the e-bike as well as the charge duration. After comparison with the normal charging pattern (see Section 3.1), the system can determine whether there is a problem with the charger and battery, thus, monitoring the e-bike's charging health.

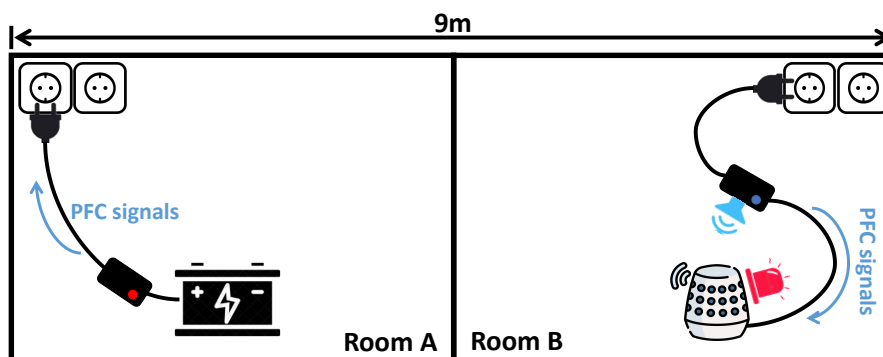


Figure 1. Diagram of the signal-propagation process. The PFC signal generated by the charger travels along the grid and affects the power supply to the smart speaker causing it to emit sound.

In developing the proposed *SingMonitor*, we encountered several challenges: (1) Interference of noises. The PFC signals are exposed to background noise interference from the power grid, the environment, the power supply's internal components, and the sound

acquisition equipment during the propagation and conversion to sound signals. PFC signals generated by other appliances can also interfere with the e-bike's PFC signal.

(2) It is difficult to distinguish different e-bikes and their charging stages in a complex appliance environment. Considering that the types, numbers, and combinations of appliances in different homes vary, we need to design a method that can be trained with only e-bike data and still perform well in complex appliance environments to improve our system's usability. (3) It is also difficult to define a healthy charging status.

We then proposed many schemes to solve these problems: (1) We proposed a noise cancellation method based on variational mode decomposition (VMD), periodicity detection, and spectral subtraction. We adopted VMD and periodicity detection to eliminate the aperiodic background noise. To obtain clean e-bike charge-stage templates (see Section 5), we employed spectral subtraction to remove the interference of other appliances. (2) We proposed a template-matching-based scheme and designed a new distance metric to distinguish different e-bikes and their charging stages.

We defined a new similarity metric by comparing the differences in center frequency and bandwidth based on the characteristic that the center frequency and bandwidth of PFC signals generated by different appliances and e-bikes' different charging stages are different. (3) We proposed to build the normal charging pattern by calculating the duration of different charging stages in the registration phase (see Section 5). The system compares the charge duration measured during the health-monitoring phase with the normal charging pattern. If the gap between the two exceeds a threshold (which is dynamically adjusted), the system considers the e-bike to be in an unhealthy charging status.

Our contributions can be summarized as follows:

1. To the best of our knowledge, we are the first to use sound emitted by the power supply to monitor e-bike charging health.
2. We propose a noise-cancellation scheme using VMD, periodicity detection, and spectral subtraction to cancel both background noise and interference from other appliances.
3. We propose a template-matching-based scheme and designed a new distance metric to distinguish different charging stages.
4. We defined healthy charging states by comparing the duration of each charging stage measured by the system with the normal charging pattern.
5. We evaluated *SingMonitor* in real-world scenarios, and our experiments show that *SingMonitor* achieved an F1 score of 0.94 in identifying 10 e-bike charging stages with a detection distance of 9 m+.

2. Related Work

In this section, we review techniques in four areas relevant to this paper, i.e., fire alarm systems, electrical appliance detection, battery monitoring, PFC, and switching-mode power supply (SMPS).

2.1. Fire Alarm System

There are many existing studies that focus on improving fire alarm systems to prevent fire disasters. For example, refs. [9–15] improved FACU's performance by changing the sensors and boosting the communication efficiency between sensor nodes. Refs. [16,17] used image-processing technology to enable the rapid detection and treatment of fires. Ref. [34] employed a camera with an optical and thermal lens for kitchen fire warnings. However, a common problem with these methods is the high installation and maintenance costs; additionally, camera-based methods may raise privacy concerns.

2.2. Electrical Appliance Detection

Many studies in appliance detection can also monitor the charging health of e-bikes. We split such research into two categories based on the channel they used.

Direct load monitoring: Such studies install sensors directly in the circuit to obtain current and voltage information. Intrusive appliance monitoring installs sensors near each

appliance. Ref. [18] integrated several types of sensors within the socket, which was used to collect the usage of nearby appliances as well as environmental data. Ref. [19] used smart plugs. However, intrusive methods are costly due to the extensive use of sensors.

There are also many methods using non-intrusive load monitoring (NALM) instead. NALM [20] typically employs only one sensor to monitor the circuit's total power consumption. This information is utilized to analyze the power consumption pattern of individual appliances and other information, such as the appliance usage time. Ref. [21] estimated the number of individual loads and their energy consumption by analyzing the voltage and current waveform of the total load. Ref. [22] analyzed household appliance power consumption patterns using a single sensor to obtain real power data. Refs. [23,24] employed current harmonics as the core feature to identify load types. Nevertheless, NALM is also difficult to use in large-scale deployment because it requires extra hardware.

Side-channel: Side-channel technology uses the various physical signals generated by appliances during their operation to enable appliance detection. For example, ElectriSense [25] utilizes electromagnetic interference (EMI) from the switching-mode power supply to obtain individual appliance usage information. Ref. [26] collected power-draw information using a mobile electromagnetic field (EMF) sensor.

Ref. [27] recognized appliances by the sounds users make when using the appliance and the sounds produced by the appliance itself. Ref. [28] correlated an appliance's inherent acoustic noise with its energy consumption pattern and collected ambient sound to obtain its energy consumption pattern. However, this method has a limited monitoring range. In addition, all these works rely on extra sensors, making them problematic for large-scale deployment.

2.3. Battery Monitoring

Many studies focus on battery monitoring. For example, ref. [29] measured the battery's voltage and temperature by installing wireless sensors inside each cell to assess the battery's state of health. Ref. [30] designed an IoT system to obtain information, such as the battery voltage, and to upload it to the control interface to help the user know of and deal with any abnormal status of the battery in time. Ref. [31] designed a battery management system using sensors to obtain parameters, such as the battery voltage, current, and temperature. These parameters were used to train an LSTM model to monitor and protect the battery status.

Ref. [32] proposed an electrochemical model that monitors the cell state by calculating parameters, such as the open-circuit voltage and liquid-phase diffusion. The calculation of these parameters relies on the readings of current, voltage, and other data. However, these methods require extra hardware to obtain data, such as the current and voltage, which raises the system cost. Compared with these direct-style monitoring methods, we propose a side-channel method that does not require the current and voltage. Furthermore, these methods are mainly for electric vehicles or lithium batteries, which are not necessarily applicable to our target.

2.4. PFC and Switching-Mode Power Supply

Many other works use PFC or SMPS signals. For example, ref. [35] found that PFC signals can precisely reveal information about devices' power-draw, and they implemented a power side-channel attack by utilizing this trait to infer computer application launching. Changes in the computer's power consumption can affect the high-frequency voltage ripple generated by its PFC circuits, and NoDE [36] exploits this phenomenon to achieve data exfiltration.

Ref. [37] attacked air-gapped, audio-gapped systems by planting malware to manipulate the computer's SMPS to emit specific frequency sounds. CapSpeaker [38] employs the capacitor's inverse piezoelectric effect to issue malicious voice commands to attack nearby smart speakers. Ref. [39] used the sound from the SMPS and other noises produced by

appliances to identify different appliances and used their locations for indoor localization. We were inspired by these works.

3. Background

In Section 1, we describe how *SingMonitor* works: The charging e-bike can inject unique PFC signals into the power grid. The PFC signals are then transmitted through the power grid. The transmitted PFC signals can drive the power supply at the other end of the grid to generate sound. The sounds can be captured by nearby mobile devices and used to monitor the charging health of e-bikes. In this section, we first discuss the causes and effects of e-bike overcharging; second, we describe why e-bikes can generate a unique PFC signal when charging; then, we describe why this PFC signal can propagate through the grid; and finally, we describe why this PFC signal can drive the power supply to produce sound.

3.1. E-Bike Overcharging and Its Causes

E-bike overcharging: E-bikes are mainly powered by lead-acid and lithium batteries, which have current market shares of 30.83% and 46.41%, respectively, [40]. Overcharging can cause e-bike battery capacity loss or even fires. Overcharging for lead-acid batteries raises the internal temperature, producing harmful gases and drying out the electrolyte, ultimately leading to positive grid corrosion.

Grid corrosion can significantly shorten the battery life; however, lead-acid batteries are generally less susceptible to fire [41]. Fires caused by overcharging typically occur on lithium batteries. Lithium batteries usually consist of a positive and negative pole material and a separator that divides the two. Overcharging can cause severe side reactions within the lithium battery, which can cause the internal separator to rupture, resulting in severe thermal runaway and, eventually, fire [42].

Causes of e-bike overcharging: E-bike chargers mainly use three-stage charging: constant current, constant voltage, and float charging. Figure 2 shows that the charger indicator is red during the constant current and constant voltage stages. In the experiments, we use an ammeter to measure the change in current to distinguish between these two stages. When the battery is charged to 80%~95%, the charger enters the float stage, and the indicator light turns green.

The charger monitors the charging current and the battery voltage via an internal feedback circuit, which decides when to switch charging stages. When the charger charges the battery with a high current or voltage for a long time due to quality problems, it cannot switch to the float stage in time and the battery will be overcharged, resulting in a loss of capacity or even a fire. Furthermore, when the battery is faulty and thus cannot reach its rated voltage during charging, the charger will continue to supply power at a high current, thus, causing the battery to overcharge.

The duration of each stage varies depending on the charger and the battery. We calculated the duration of each charging stage during initialization (see Section 5) to build the normal charging pattern for the corresponding e-bike. Long-term float charging is generally harmless, and we are more concerned with the duration of the constant-current and constant-voltage stages.

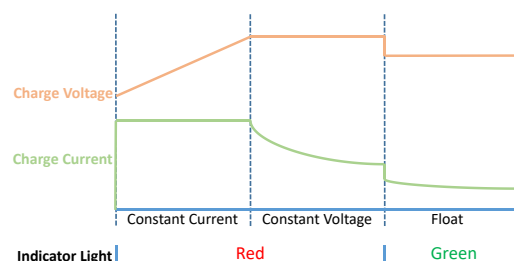


Figure 2. Three-stage charging.

3.2. E-Bike Charging Generates Unique Power Factor Correction Signals

In this section, we explain why e-bike charging can generate unique PFC signals.

Power factor (PF): In electrical engineering, the power factor is defined as the ratio between the real power consumed by a load and the total real-plus-reactive power, which is also known as the total apparent power [43], i.e., $PF = P_{real} / P_{apparent}$. Figure 3 shows that the PF can reach 1 when the input current can follow the instantaneous line voltage without distortion. This means that the total apparent power is the lowest while consuming the same real power, thus realizing the most efficient use of electrical energy. In other cases, the PF is less than 1, meaning that electrical energy is wasted in the distribution system.

Power factor correction (PFC): PFC circuits [44] can increase the PF to reduce power losses by eliminating high harmonics through low-pass filters or by shaping the input current. Therefore, PFC circuits are required in many types of electrical appliances. According to the IEC61000-3-2 standard [45], PFC circuits are required in power adapters for lighting devices with more than 5 W and Class D devices with more than 75 W. The PFC circuit in e-bike chargers is implemented by a pulse width modulator (PWM). A PWM modulates the current by periodically generating high-frequency ripples to make the input current follow the instantaneous line voltage.

The modulation of the input current by PFC circuits injects feedback currents into the grid, i.e., PFC signals. The research [35] shows that load power consumption information can modulate the amplitude and frequency of PFC signals. The features of PFC signals can also be affected by the design and manufacturing process of PFC circuits. Therefore, as shown in Figure 4, there are distinct differences in the spectrum of the PFC signals generated by different e-bikes, appliances, and charging stages of the same e-bike. As of the difference between PFC signals, *SingMonitor* can accurately analyze whether e-bikes are charging and which charging stage they are in from the mixed PFC signals generated by multiple appliances.

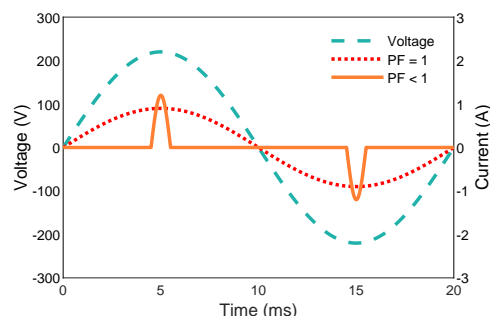


Figure 3. Effect of the current waveform on the power factor.

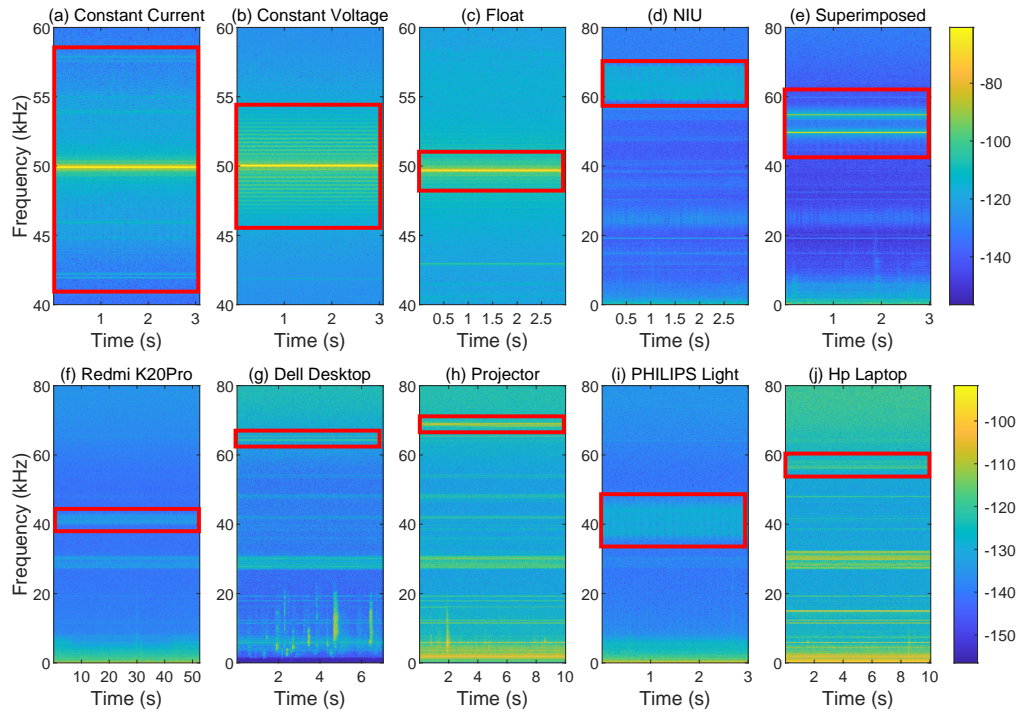


Figure 4. PFC signals generated by different e-bikes and appliances: (a–c) Generated by the XDAO (160 W) e-bike during different charging stages. (d) Generated by the NIU (160 W) e-bike during the constant current stage. (e) The superimposed signal generated when YADEA (180 W) and XDAO work simultaneously. (d–f) Generated by Redmi K20Pro (27 W), Dell desktop (360 W), Projector (225 W), PHILIPS Light (18 W), and HP Laptop (90 W), respectively.

3.3. Propagation of PFC Signals in the Power Grid

This section explains how PFC signals propagate through the grid. A typical household grid consists of a distribution box and multiple distributed sockets with appliances connected in parallel. Figure 5 is an abstract illustration of a typical household grid. For the convenience of discussion, we assume that two sockets are connected to the e-bike battery or the smart speaker.

The following will explain how the current I_0 containing the PFC signal affects the input current I_x of the smart speaker, where V_s denotes the source voltage of the grid, I_i is the input current of each branch, R_s is the resistance of the common wire through which all currents flow, R_x is the resistance of the wire connected to the smart speaker, and R_a is the internal resistance of the smart speaker. Each branch has its line resistance, and we have labeled only the line resistance R_x used in Equation (1). The relationship between the input current of the smart speaker, the source voltage, and the current of each branch is as follows:

$$\begin{aligned} V_s &= \left(\sum_{i=0}^n I_i + I_x \right) R_s + I_x (R_a + R_x) \\ I_x &= \frac{V_s}{R_s + R_x + R_a} - \frac{R_s}{R_s + R_x + R_a} \sum_{i=0}^n I_i \end{aligned} \quad (1)$$

Clearly, the input current of the smart speaker I_x is influenced by the current of the other branch I_i . As mentioned in Section 3.2, PFC signals (feedback current) are part of I_i . When the input current of the smart speaker I_x is influenced by I_i , it is influenced by the PFC signals generated by other branches.

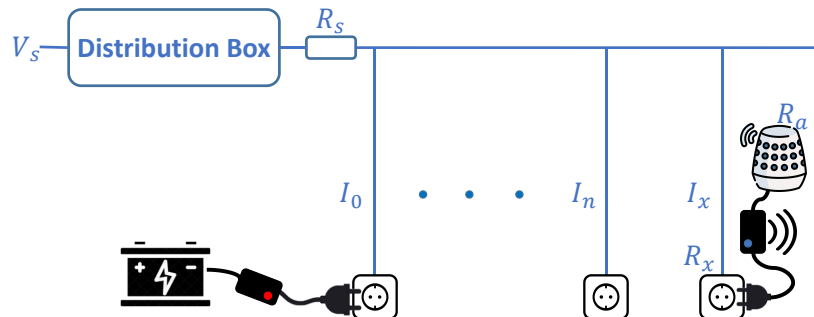


Figure 5. Illustration of the household grid.

3.4. Transmitted PFC Signals Can Drive the Power Supply to Generate Sounds

This section explains how I_x , which contains the PFC signals, causes the power supply to emit sound. A typical power supply contains multiple capacitors and inductors inside. When current flows through the power supply, these capacitors and inductors generate sound signals under the action of the current. For example, Figure 6 shows a typical inductor, which consists of a magnetic core and a coil wound on it.

A changing current produces a changing magnetic field, and the core is repeatedly stretched in the direction of magnetization to produce sound, a phenomenon known as magnetostriction [46]. Figure 7 shows a capacitor. When a high-frequency current acts on the capacitor, the capacitor deforms. This phenomenon is called the inverse piezoelectric effect. The deformation of the capacitor acts on the circuit board to produce sound. In a preliminary study, we also observed that the sound generated by the power supply is consistent with the PFC signals in terms of features (see Section 4.3).

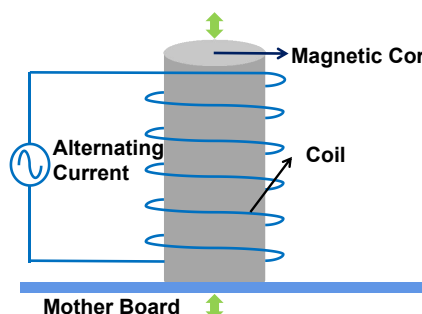


Figure 6. Magnetostriction of a magnetic core under the influence of alternating current.



Figure 7. A capacitor exhibits an inverse piezoelectric effect due to the electric field.

4. Preliminary Study

In Section 3, we showed that e-bike charging can generate a special PFC current that can drive the power supply in the grid to generate sound from a distance. Before we can use this principle for e-bike charging health monitoring, we need to answer the following questions: (1) Are the PFC currents unique for each e-bike and the different states of e-bikes? (2) Are the PFC currents stable over time? (3) Can the transmitted PFC currents generate sounds of the same frequency?

We conducted a preliminary study in two rooms (rooms A and B; see Figure 1) under a household grid to answer these questions. In Room A, we connected different appliances or e-bikes to the grid (listed in Tables 1 and 2). In Room B (see Figure 11), we connected a Tmall smart speaker to the grid and used a sound card with a maximum sampling rate of

192 kHz to receive the sound signal from the smart speaker's power supply. At the same time, we captured the PFC signal (current) with an ACS712 current sensor and Analog Discovery2 (AD2).

Table 1. E-bikes used in the preliminary study (marked with *) and the evaluation data.

Brand	Model	Battery Type	Power Rating (W)
YADEA (a) *	DE2	Lithium	180
YADEA (b)	TDT1241Z	Lithium	160
AIMA *	D260TZA-L4812	Lithium	110
NIU *	UQis	Lithium	160
FOREVER *	Sport	Lead-acid	120
XDAO *	XiaoK	Lead-acid	160
PALLA	K11	Lithium	210
SUNRA	TDT4960Z	Lead-acid	110
AiSUN	LOLLIPOP	Lead-acid	120
Lvliang	TDR183Z	Lead-acid	175

Table 2. Appliances used in the preliminary study and evaluation.

Type	Brand-Number (Power Rating)
Light	Xiaomi-2 (9 W, 9 W); PHILIPS-1 (18 W)
Projector	Sony-1 (225 W)
Monitor	PHILIPS-1 (21 W); Dell-1 (50 W)
Laptop	Hp-2 (65 W, 90 W); Lenovo-1 (65 W)
Phone charger	Huawei-1 (40 W); Xiaomi-2 (33 W, 35 W)

4.1. Uniqueness

To answer Question 1, we used AD2 to collect multiple data segments at the different charging stages of each e-bike with each lasting for 20 s. Similarly, we also collected the PFC signals of the remaining 12 electrical appliances. We performed 2D correlation analysis on the spectrograms of these data [47]. Figure 8 shows the cumulative distribution function (CDF) of the correlations. The correlations between different e-bikes and different appliances do not exceed 0.69, and the correlations between different charging stages of the same e-bike do not exceed 0.77. The experiments demonstrated that the differences between PFC signals are sufficient to distinguish between different appliances and e-bike charging stages.

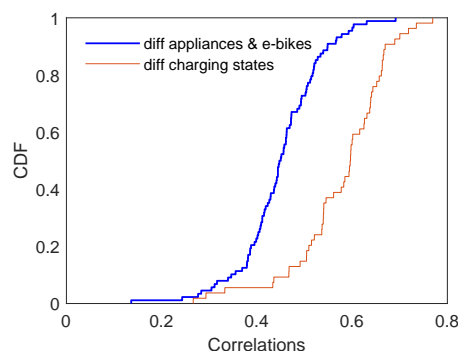


Figure 8. Blue is the CDF of the 2D correlation between different appliances and e-bikes (including different charging stages). Orange is the CDF of the 2D correlation between different charging states of the same e-bike.

4.2. Stability

To answer Question 2, for each e-bike, a set of data was collected every 5 days using AD2 with each set containing multiple data segments from three charging stages and each

segment lasting 20 s, and we collected these data over 1 month. We then performed a 2D correlation analysis between the same charging states of the same charger by using the first set of data as a benchmark. We averaged the correlations for the different charging stages of the same e-bike and averaged the correlations for other appliances. Figure 9 shows that the correlation between PFC signals can always be maintained above 0.94 within a month, which suggests that the PFC signals remained stable over time.

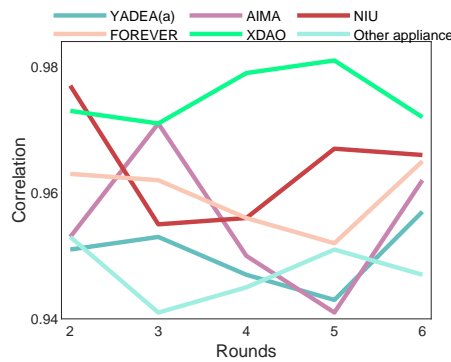


Figure 9. 2D correlation of five rounds over a period of 30 days.

4.3. Consistency

To answer question 3, in Room A, we connected an HP laptop to the grid. Then, in Room B, we simultaneously measured the sound signals generated by the power supply and the PFC signal (current). Figure 10 shows the power spectrum of the current and the corresponding sound signal, both of which have identical frequency spikes at 21.28 kHz. To better present the information in the power spectrum, we took the logarithm of the vertical axis in conjunction with the definition of decibels ($N_{dB} = 10 \lg(P_x/P_0)$, and P_0 is the custom reference value); therefore, the vertical axis unit in Figure 10 is dB. This shows that the sound signal generated by the power supply is characteristically consistent with the corresponding current signal.

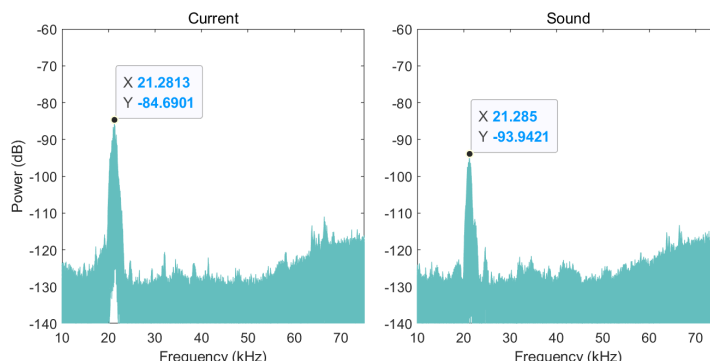


Figure 10. Spectrum of the simultaneously collected current and sound signals.

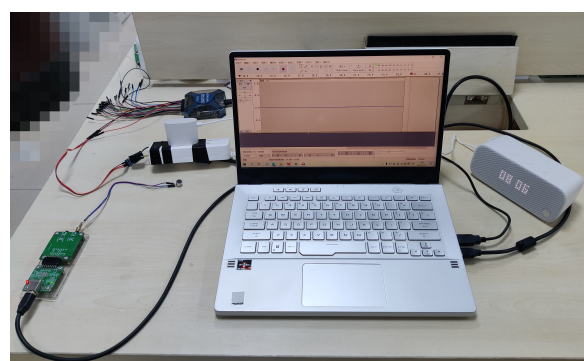


Figure 11. Image of the data collection equipment.

5. System Design

As shown in Figure 12, the proposed system comprises two phases: the registration phase and health-monitoring phase.

Each e-bike needs to be registered individually. During the registration phase, the e-bike must undergo a complete charging cycle, during which the system continuously collects the sound signals generated by the power supply. As the background sound can be collected before the e-bike is connected to power in the registration phase, the registration phase can use spectral subtraction to weaken the background noise and the interference from other appliances' PFC signals.

Combined with VMD and periodicity detection, we can obtain a signal containing only information about the e-bike charging stage. This signal will be used to generate the charging stage template. The system compares the template information obtained at different times to determine the current charging stage and calculates the duration of each charging stage, thereby, generating the normal charging pattern of the corresponding e-bike. The system can register different models of e-bikes on the market in advance for users' convenience.

In the health-monitoring phase, the system first preprocesses the data to remove background noise and then obtains a sound signal that may contain the PFC features of multiple appliances and e-bikes. By matching the template information obtained in the registration phase, the system can determine which e-bikes are charging in the grid and what charging stage they are in. The system can obtain the duration of the constant current and constant voltage stages from the charging stage information collected many times. After comparing this with the normal charging mode, the system can judge whether these two stages' durations are normal in order to analyze the e-bike's charging health.

In the following sections, we will present these phases in detail.

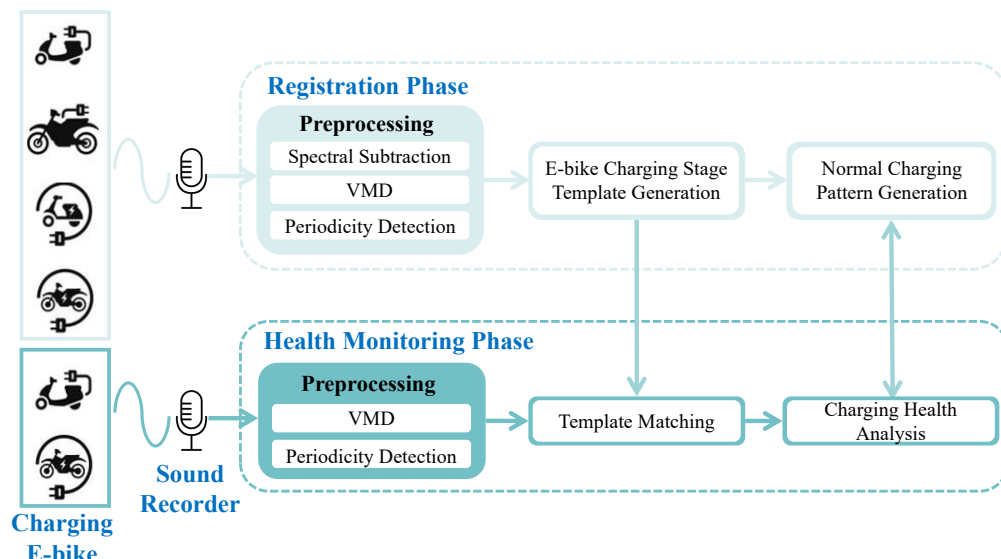


Figure 12. System overview of *SingMonitor*.

6. Methodology

In this section, we present the methods used by the system.

6.1. The Registration Phase

6.1.1. Spectral Subtraction

To generate a better e-bike charging stage template, our first step is to improve the signal-to-noise ratio. As the noise in the system changes relatively slowly and the PFC signals generated by other appliances can remain stable, it is well suited for processing the

signal by spectral subtraction [48] to obtain cleaner template information. The sound signal S_r received by the microphone can be expressed as follows:

$$S_r = S_{pfc}(\omega_0) + N_{bg+opfc} \quad (2)$$

where $S_{pfc}(\omega_0)$ refers to the sound signal generated by the influence of the e-bike PFC signal, and ω_0 is the central frequency of the signal. $N_{bg+opfc}$ is the background noise (including the ambient noise, the internal noise of the power supply, and the sound card's noise floor) and interference from other appliances' PFC signals. $N_{bg+opfc}$ is time-invariant and follows a specific distribution. Thus, we can attenuate $N_{bg+opfc}$ with spectral subtraction:

$$\hat{S}_{pfc}(\omega_0) = F^{-1}[|S_r| - E[|N_{bg+opfc}|]]e^{j\theta}] = S_{pfc}(\omega_0) + \epsilon \quad (3)$$

where $E[|N_{bg+opfc}|]$ represents the estimated background noise and interference, F^{-1} is the inverse fast-Fourier transform, θ is the original phase, and ϵ is the estimation error.

6.1.2. Variational Mode Decomposition

We further processed the signal to extract PFC features. As the center frequency of the PFC signals can remain stable, we can use variational mode decomposition (VMD) to further process the data. VMD can decompose the sound signal into several narrow band components, i.e., intrinsic mode functions (IMFs).

We use VMD to divide $\hat{S}_{pfc}(\omega_0)$ into k narrow band signals (denoted by $u_k(\omega_0)$), and ω_k is an estimate of the corresponding signal center frequency. We calculated the penalty term after converting the narrow-band signal from the pass band to the base band. Therefore, the optimization objective in the frequency domain is as follows:

$$\begin{aligned} \min_{u_k(\omega_0)} & \{ || \sum_k u_k(\omega_0) - \hat{S}_{pfc}(\omega_0) ||_2^2 + \alpha \sum_k || j(\omega_0 - \omega_k) u_k(\omega_0) ||_2^2 \} \\ \text{s.t. } & \sum_k u_k(\omega_0) = \hat{S}_{pfc}(\omega_0) \end{aligned} \quad (4)$$

where α is the penalty factor. To guarantee fidelity when reconstructing the sound signal, we added a restriction: $\sum_k u_k(\omega_0) = \hat{S}_{pfc}(\omega_0)$. The optimal solution can be obtained using the Lagrange multiplier, which is followed by the alternating direction method of multipliers algorithm to locate the saddle point [49].

6.1.3. Periodicity Detection

After VMD, the received sound signals were decomposed into several IMFs; however, we need to remove the IMF associated with background noise. We noticed that the background noise is an aperiodic random signal; however, the PFC feature is periodic, which allows us to further reduce the noise using periodicity detection.

To determine the periodicity of IMFs, we first calculated the upper envelope of each IMF and then derived the corresponding autocorrelation coefficient. Then, we divided each IMF into segments, where the autocorrelation coefficient's peak determines each segment's starting point. The length of each segment should exceed the fundamental period of the corresponding IMF, which we set empirically to 0.05 s. Finally, we computed the Pearson correlation coefficient (PCC) between segments, and we considered an IMF as periodic when its average PCC reached a set threshold.

6.1.4. Template Generation

After preprocessing, we obtained clean sound signals. For each charging stage k of the e-bike l , the corresponding processed sound signal is denoted as signal S_{kl} . We used the short-time Fourier transform (STFT) with a Hanning window (4096 points) with a shifting interval of 441 points. For window m , the corresponding spectrogram is denoted

as $S'_{kl,m}$. We then generated a template for real-time traces to match with. The process can be expressed as follows:

$$T_{kl} = \frac{1}{M} \sum_{m=1}^M (S'_{kl,m}) \quad (5)$$

where T_{kl} is the generated template and M is the number of windows. In this paper, the time length M of the templates is set to 200 frames. The templates are then preserved for matching the real-time collected sounds.

6.1.5. Normal Charging Pattern Generation

The system records when the templates are generated and compares the templates obtained at different times to obtain the duration of each charging stage (*SingMonitor* is mainly concerned with the duration of the constant current and constant voltage stage). The system uses the above information to build the normal charging mode of the corresponding e-bike, which will be used for the charging health analysis in the health-monitoring phase.

6.2. The Health-Monitoring Phase

In the registration phase, we obtained templates for different charging stages of various e-bikes under laboratory conditions and built the normal charging pattern of the corresponding e-bike. In this section, we introduce the preprocessing of sound data collected by the user, the template-matching method, and how to use the normal charging pattern to judge the charging health.

6.2.1. Preprocessing

As in the registration phase, the sound data captured by the user also contains noise and, therefore, needs to be processed for noise reduction. However, unlike the registration phase, we do not require users to collect background sounds in advance. Therefore, only the VMD and periodicity detection will be used for noise reduction in the registration phase. S'_r represents the sound signal captured directly by the user, and the corresponding sound signal after preprocessing is $\hat{S}_{pfc}(\omega_0)'$.

6.2.2. Template Matching

In developing this metric, we considered two factors in combination.

The center frequency similarity: The center frequency varies significantly between different appliances and e-bikes (as mentioned in Section 3); Therefore, we developed the measure $D1$. This considers the difference between the center frequencies of the target and the template as measured using the Euclidean distance. First, since different frequency components in the template have different impacts on the matching, we constructed a weight for each frequency component, denoted as ω_1 . The weight function ω_1 is defined as:

$$\omega_1 = F_D(f) T_{kl}(f) \quad (6)$$

where T_{kl} is the template and F_D is a filter function. Then, the distance can be determined by integrating the local distance γ_i in the time-frequency domain, weighted by ω_1 , which can be expressed as:

$$D1_i = \sum_{t=1}^{10} \sum_{f=1}^{2048} \omega_1 \gamma_i(t, f) \quad (7)$$

The frequency width similarity: During the experiments, we found that the similarity of the central frequency was not the only factor that influenced the template-matching procedure. For example, the difference between the different charging states of the same e-bike was more clear in the bandwidth. To measure this metric, similarly, we developed the evaluation metric $D2$, which is expressed as follows:

$$D2_i = \sum_{t=1}^{10} \sum_{f=1}^{2048} \omega_2 width_i(t, f) \quad (8)$$

where $width_i$ is the frequency width of each frequency band, defined as the frequency components that are larger than $0.2 \times f_{max(i)}$, and $f_{max(i)}$ is the max strength of the center frequency of this frequency band. Ten frames (a frame is the window size in the STFT) of data are used for template matching.

We then combined these two metrics to measure the similarity of the template and the actually acquired signal:

$$D_i = D1_i + \lambda D2_i \quad (9)$$

where λ is the penalty factor, which ranges from 0 to 1. λ is tuned in the registration phase and applied in the monitoring phase.

6.2.3. Charging Health Analysis

When the system starts, the duration of all charging states is set to 0. The system collects sounds at time interval ΔT , obtains which e-bikes are charging and their charging stages by template matching, and then adds ΔT to the duration of the corresponding charging stage. If a charging state has not been detected for a long time, its duration is reset to 0.

The system compares the duration of the constant current and constant voltage stage with the normal charging pattern of the corresponding e-bike. Once the duration of the constant current and constant voltage phase significantly exceeds the duration in the normal charging pattern (in the actual experiment, the threshold was set to 30%), the system considers that there is a fault with the e-bike battery or charger and provides a warning about its charging health. The system will use the data measured during the health-monitoring phase to adjust the threshold of the corresponding e-bike.

7. Evaluation

7.1. Experiment Setup

7.1.1. Experiment Setup

As shown in Figure 1, we conducted experiments in two rooms under a distribution box. The distance between the sockets in the two rooms was 9 m. At the receiving end (room B), we used the Tmall smart speaker's power supply to generate the sound signal. Since the smart speaker's internal data is unavailable, we chose a sound card (connected to an electret condenser microphone) with a maximum sampling rate of 192 kHz to capture the sound signal (see Figure 11). At the PFC signals transmitting side (room A), we used a total of 10 e-bikes and 12 other appliances for the experiment (see Tables 1 and 2). Furthermore, we used an ACS712 current sensor to obtain the charging stage of the e-bike and used this as the ground truth.

7.1.2. Dataset Preparation

A total of three datasets were generated in the experiments for the micro benchmark, overall evaluation, and robustness evaluation.

Registration Dataset: For the register phase, we used 10 e-bikes in the experiments. We conducted multiple 30 s data collections for each charging stage of each e-bike, with a total data length of 90 min, of which we chose the first 20 s to generate templates and the last 10 s to perform template matching and to obtain a micro-benchmark of the system.

Overall Dataset: For the health-monitoring phase, we conducted a real-world experiment by randomly connecting multiple e-bikes and other appliances in Room A (up to three e-bikes and four other appliances working simultaneously). To reduce the system complexity, we collected 0.5 s of sounds every 15 min (as mentioned in Section 6.2.2, 0.25 s of data was enough for the system to perform a template match). We experimented for 25

days, and the total duration of the data collected during the experiment was 381 s. These data were used to evaluate the overall system performance (see Section 7.3).

Robustness Dataset: Similarly, to evaluate the robustness of *SingMonitor* (see Section 7.4), five e-bikes were used in the experiment (e-bikes marked with * in Table 1). We experimented on each e-bike under different influencing factors and averaged the results to measure the system's performance. The corresponding total data length was 620 s.

7.1.3. Evaluation Metric

As mentioned in Section 3.1, *SingMonitor* mainly uses the constant current/voltage stage duration to determine whether the e-bike is in a healthy charging status. Therefore, we mainly evaluated the accuracy of the system for classifying the different charging stages of different e-bikes. The $F1_i$ score was used to assess each class's performance, and the micro $F1$ score was used to measure the overall system performance. $F1_i$ can be computed as follows:

$$F1_i = \frac{2 \cdot p_i \cdot r_i}{p_i + r_i} \quad (10)$$

where p_i and r_i are the precision and recall for a particular charging state of an e-bike, respectively. Essentially, the $F1_i$ score and micro $F1$ score are positively correlated with the system's classification performance. In addition, we evaluated the overall system performance in Section 7.3 by counting the duration of the different charging phases.

7.2. Micro-Benchmark

This section evaluates how different parameters affected the *SingMonitor* performance. The registration dataset was used for evaluation.

7.2.1. STFT Window Size

The window size in STFT determines the resolution of the spectrogram. The time resolution of the spectrogram decreases as the window size increases, while the frequency resolution does the opposite. The time-frequency resolution affects the template generation and matching, thereby, affecting the system performance. We experimented to select the best window size. Figure 13a shows the micro $F1$ score for different window sizes, and we finally choose 4096 (micro $F1$ score of 0.97) as the window size for STFT.

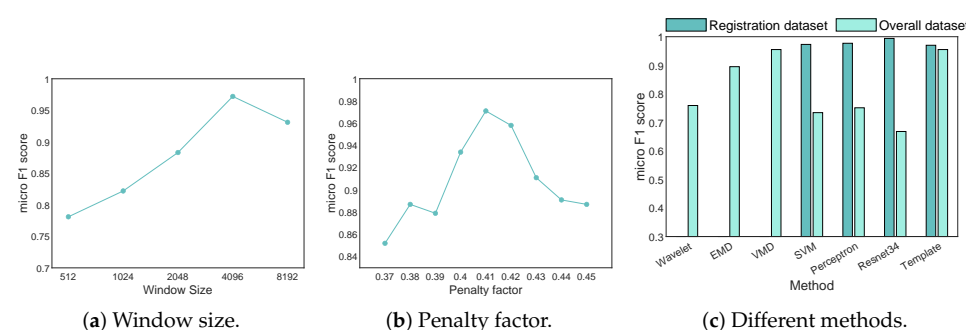


Figure 13. Performance of *SingMonitor* with different micro-benchmarks.

7.2.2. Penalty Factor λ

The penalty factor (see Section 6.2.2) is used to adjust the weighting of the central frequency similarity to the frequency width similarity. We experimented to determine the size of this value. Figure 13b shows that the system performed best when the penalty factor was 0.41 (the micro $F1$ score was 0.97), so we used 0.41 as the penalty factor in all subsequent experiments.

7.2.3. Different Methods

Different noise reduction schemes and different classification methods will have an impact on the system performance. We changed the preprocessing method to wavelet transform and empirical mode decomposition (EMD) combining wavelet threshold, which we tested using the overall dataset. Figure 13c shows that the variational mode decomposition (VMD) method performed best. We also used SVM, multi-layer perceptron, and resnet-34 models to classify e-bikes and their charging stages. The registration dataset was used to train and test these models, and the overall dataset was used for testing only.

As shown in Figure 13c, in the registration dataset, all of these models performed well. However, because the overall dataset was interfered with by the PFC signals generated by other appliances, the performance of these models on the overall dataset degraded to varying degrees. The template matching was designed based on the characteristic that the center frequency and bandwidth of PFC signals generated by different appliances and e-bikes' different charging stages are different. Thus, it is more resistant to interference and performs more stably.

7.3. Overall Performance

In this section, we evaluate the overall performance of *SingMonitor*. The overall dataset was used for evaluation.

7.3.1. Template Matching Evaluation

As mentioned in the evaluation procedure, during the experiment, the system collected a 0.5 s sound signal every 15 min and performed template matching to determine which e-bikes were charging in the grid and what charging stage they were in. Figure 14a shows that the F1 score reached above 0.94 for different charging stages of different e-bikes. This proves that the system can achieve high performance in a complex environment with multiple e-bikes and other appliances.

7.3.2. Duration of Charging Stages

The system calculates the durations of different charging stages and compares them with the normal charging pattern of the corresponding e-bike to judge the charging health. During the experiments, the duration of the constant current and constant voltage stages was within the normal range for all 10 e-bikes, and the system judged the charging health of these e-bikes to be fine. As shown in Figure 14b, we cumulated the duration of the different phases of each e-bikes and compared with the real time data (the system does not care about the duration of the float stage; however, it can also be calculated). The error between the system calculation time and the real time did not exceed 9%. The time calculated by the system is high compared to the real time because the system's misjudgment of the charging stage tends to increase the charging time.

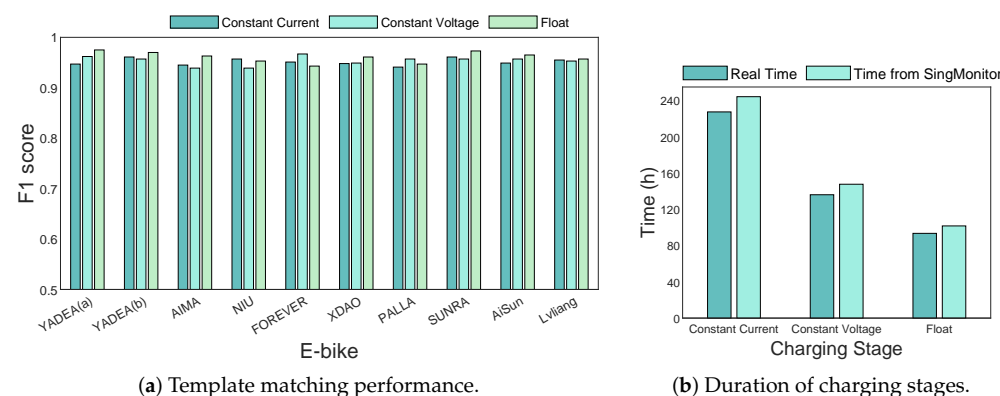


Figure 14. The overall performance of *SingMonitor*.

7.4. Robustness

In this section, we evaluate the robustness of *SingMonitor* under different influences. The robustness dataset was used for evaluation.

7.4.1. Impact of the Number of Appliances

We gradually increased the number of other types of appliances in the grid (1~10) to evaluate the system. Figure 15a shows that, as the number of appliances increased, the system's performance decreased. This is because the increase in the number of appliances made the PFC signal generated by e-bikes more susceptible to interference in the frequency domain, which affects the template matching. When the number of appliances did not exceed six, the micro F1 score was maintained above 0.9.

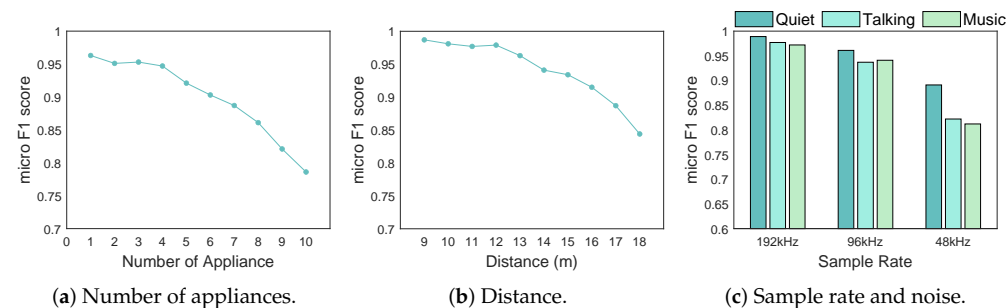


Figure 15. The robust performance of *SingMonitor*.

7.4.2. Impact of Distance

We increased the propagation distance of the PFC signals by extending the wires. As shown in Figure 15b, the system performance decreased with increasing distance because the strength of the PFC signal gradually attenuated as the propagation distance increased. However, the micro F1 score was still maintained above 0.91 in the range of 16 m.

7.4.3. Impacts of the Sound Sampling Rate and Environmental Noise

Aliasing errors occur when the sampling rate does not meet the Nyquist sampling theorem. We varied the sample rate (192, 96, and 48 kHz) of the sound card and conducted experiments with different environmental noises (quiet, talking, and playing music) to verify the effects of the sample rate and noise on the system. Figure 15c shows that the system's performance deteriorated as the sampling rate decreased and the noise increased. Regarding the aliasing effect, we can extract distorted PFC features at low sampling rates, so the system can still work at low sampling rates (the micro F1 score at 48 kHz was 0.89). At low sampling rates, the effect of noise on the system was more pronounced because the noise could not be completely removed, and its frequency was lower, which makes it more likely to interfere with the distorted PFC features.

8. Discussion

SingMonitor is limited by several issues. First, the microphones of mobile devices, such as smartphones, often use low-pass filtering, i.e., an anti-alias filter (AAF), before sampling the audio signals. Due to the AAF, mobile devices may not be able to capture clear PFC frequencies, thus, affecting *SingMonitor*'s performance. However, existing studies have attempted to recover the signals that underwent AAF processing using methods such as non-linearity [50], and we will subsequently test these methods.

Second, the center frequency of certain electrical appliances is close to that of e-bikes, which may affect the monitoring of e-bikes when these devices are in use. In particular, some appliances (such as air conditioners, laundry machines, and refrigerators) change their frequency when operating, causing the appliance noise removal method based on spectral subtraction to fail and reducing the system's performance.

However, these devices are few in daily life. In addition, we can also use other methods (e.g., low-frequency sound) and the sound of the user using the appliance as compensation for classification, or we can collect and analyze their signal characteristics in advance to remove their interference on the system.

9. Conclusions

To the best of our knowledge, we are the first to use sounds emitted by the power supply to monitor e-bike charging health. Compared with existing fire warning systems or other e-bike-monitoring systems, *SingMonitor* uses power supplies everywhere for monitoring, which can be implemented on mobile devices and can achieve long-range monitoring.

A noise-cancellation scheme combining VMD, periodicity detection, and spectral subtraction was used to cancel background noise and the interference from other appliances. We proposed a template-matching-based scheme and designed a new distance metric to distinguish different charging stages. Experiments showed that *SingMonitor* achieved an F1 score of 0.94 in identifying 10 e-bike charging stages, with a detection distance of 9 m+.

Author Contributions: Conceptualization, X.J., Y.L. and Y.-C.C.; Methodology, X.J. and L.Y.; Software, X.J.; Supervision, Y.-C.C. and G.X.; Validation, X.J. and L.Y.; Writing—original draft, X.J. All authors have read and agreed to the published version of the manuscript.

Funding: This research received no external funding.

Institutional Review Board Statement: Not applicable.

Informed Consent Statement: Not applicable.

Data Availability Statement: The data involved in this study are available upon reasonable request. The data are not publicly available because they are part of further research.

Acknowledgments: This research received no external funding.

Conflicts of Interest: The authors declare no conflict of interest.

References

1. Grand-View-Research. E-bikes Market Size, Share & Trends Analysis Report. 2022. Available online: <https://www.grandviewresearch.com/industry-analysis/e-bikes-market-report> (accessed on).
2. Net, X. National Shooting Observation. 2022. Available online: <https://www.163.com/dy/article/GSS2BJJA05169LPK.html> (accessed on).
3. CPSC. E-Bikes Recalled Due to Fire, Explosion and Burn Hazards; Distributed by Ancheer. 2022. Available online: <https://www.cpsc.gov/Recalls/2023/E-Bikes-Recalled-Due-to-Fire-Explosion-and-Burn-Hazards-Distributed-by-Ancheer> (accessed on).
4. Lei, L. Study on the Fire Risk Assessment of the Electric Bicycle Based on the AHP. In Proceedings of the 2014 seventh International Conference on Intelligent Computation Technology and Automation, Changsha, China, 25–26 October 2014; pp. 729–732. <https://doi.org/10.1109/ICICTA.2014.177>.
5. Hsieh, M.; Lai, M.; Sim, H.; Lim, X.; Fok, S.; Joethy, J.; Kong, T.; Lim, G. Electric scooter battery detonation: A case series and review of literature. *Ann. Burn. Fire Disasters* **2021**, *34*, 264.
6. Sen, C.; Kar, N.C. Battery pack modeling for the analysis of battery management system of a hybrid electric vehicle. In Proceedings of the 2009 IEEE Vehicle Power and Propulsion Conference, Dearborn, MI, USA, 7–11 September 2009; pp. 207–212. <https://doi.org/10.1109/VPPC.2009.5289848>.
7. Lee, S.; Kim, J.; Lee, J.; Cho, B.H. State-of-charge and capacity estimation of lithium-ion battery using a new open-circuit voltage versus state-of-charge. *J. Power Sources* **2008**, *185*, 1367–1373.
8. Telgian. Guide to Fire Alarm Systems. 2020. Available online: <https://www.telgian.com/fire-alarm-systems-guide/> (accessed on).
9. Kun, Z.; Shunbin, H.; Jinfang, L. Automatic Fire Alarm System Based on MCU. In Proceedings of the 2010 International Conference on Electrical and Control Engineering, Wuhan, China, 25–27 June 2010; pp. 517–520. <https://doi.org/10.1109/iCECE.2010.133>.
10. Waworundeng, J.M.S.; Kalalo, M.A.T.; Lokollo, D.P.Y. A Prototype of Indoor Hazard Detection System using Sensors and IoT. In Proceedings of the 2020 second International Conference on Cybernetics and Intelligent System (ICORIS), Manado, Indonesia, 27–28 October 2020; pp. 1–6. <https://doi.org/10.1109/ICORIS50180.2020.9320809>.
11. Muheden, K.; Erdem, E.; Vançin, S. Design and implementation of the mobile fire alarm system using wireless sensor networks. In Proceedings of the 2016 IEEE 17th International Symposium on Computational Intelligence and Informatics (CINTI), Budapest, Hungary, 17–19 November 2016; pp. 243–246. <https://doi.org/10.1109/CINTI.2016.7846411>.
12. Dong, W.h.; Wang, L.; Yu, G.z.; Mei, Z.b. Design of wireless automatic fire alarm system. *Procedia Eng.* **2016**, *135*, 413–417.
13. Azmil, M.S.A.; Ya'Acob, N.; Tahar, K.N.; Sarnin, S.S. Wireless fire detection monitoring system for fire and rescue application. In Proceedings of the 2015 IEEE 11th International Colloquium on Signal Processing & Its Applications (CSPA), Kuala Lumpur, Malaysia, 6–8 March 2015; pp. 84–89.
14. Gupta, S.; Mudgil, A.; Bhardwaj, P.; Gupta, M. Design and development of automatic fire alert system. In Proceedings of the 2016 eighth International Conference on Computational Intelligence and Communication Networks (CICN), Tehri, India, 23–25 December 2016; pp. 632–636.
15. Mahgoub, A.; Tarrad, N.; Elsherif, R.; Al-Ali, A.; Ismail, L. IoT-Based Fire Alarm System. In Proceedings of the 2019 Third World Conference on Smart Trends in Systems Security and Sustainability (WorldS4), London, UK, 30–31 July 2019; pp. 162–166. <https://doi.org/10.1109/WorldS4.2019.8904001>.
16. Sunitha, P.; Joy, K. Deep CNN-based fire alert system in Video Surveillance Networks. In *Computational Vision and Bio-Inspired Computing*; Springer: Berlin/Heidelberg, Germany, 2021; pp. 599–615.
17. Bayoumi, S.; AlSobky, E.; Almohsin, M.; Altwaim, M.; Alkaldi, M.; Alkahtani, M. A Real-Time Fire Detection and Notification System Based on Computer Vision. In Proceedings of the 2013 International Conference on IT Convergence and Security (ICITCS), Macao, China, 16–18 December 2013; pp. 1–4. <https://doi.org/10.1109/ICITCS.2013.6717783>.
18. Lifton, J.; Feldmeier, M.; Ono, Y.; Lewis, C.; Paradiso, J.A. A platform for ubiquitous sensor deployment in occupational and domestic environments. In Proceedings of the sixth International Conference on Information Processing in Sensor Networks, Cambridge, MA, USA, 25–27 April 2007; pp. 119–127.
19. Paradiso, F.; Paganelli, F.; Luchetta, A.; Giuli, D.; Castrogiovanni, P. ANN-based appliance recognition from low-frequency energy monitoring data. In Proceedings of the 2013 IEEE 14th International Symposium on “A World of Wireless, Mobile and Multimedia Networks” (WoWMoM), Madrid, Spain, 4–7 June 2013; pp. 1–6. <https://doi.org/10.1109/WoWMoM.2013.6583496>.
20. Dan, W.; Li, H.X.; Ce, Y.S. Review of Non-intrusive Load Appliance Monitoring. In Proceedings of the 2018 IEEE third Advanced Information Technology, Electronic and Automation Control Conference (IAEAC), Chongqing, China, 12–14 October 2018; pp. 18–23. <https://doi.org/10.1109/IAEAC.2018.8577910>.
21. Hart, G. Nonintrusive appliance load monitoring. *Proc. IEEE* **1992**, *80*, 1870–1891. <https://doi.org/10.1109/5.192069>.
22. Zeifinan, M.; Akers, C.; Roth, K. Nonintrusive appliance load monitoring (NIALM) for energy control in residential buildings. *Energy Efficiency Domest. Appliances Light.* **2011**, *20*, 24–26.
23. Suzuki, K.; Inagaki, S.; Suzuki, T.; Nakamura, H.; Ito, K. Nonintrusive appliance load monitoring based on integer programming. In Proceedings of the 2008 SICE Annual Conference, Tokyo, Japan, 20–22 August 2008; pp. 2742–2747.

24. Chan, W.L.; Thus, A.T.; Lai, L. Harmonics load signature recognition by wavelets transforms. In Proceedings of the DRPT2000. International Conference on Electric Utility Deregulation and Restructuring and Power Technologies. Proceedings (Cat. No. 00EX382), London, UK, 4–7 April 2000; pp. 666–671.
25. Gupta, S.; Reynolds, M.S.; Patel, S.N. ElectriSense: Single-Point Sensing Using EMI for Electrical Event Detection and Classification in the Home. In Proceedings of the 12th ACM International Conference on Ubiquitous Computing, (UbiComp’10), Copenhagen, Denmark, 26–29 September 2010; Association for Computing Machinery: New York, NY, USA, 2010; pp. 139–148. <https://doi.org/10.1145/1864349.1864375>.
26. Kulkarni, A.S.; Welch, K.C. A mobile EMF sensor for appliance identification. In Proceedings of the SoutheastCon 2016, Norfolk, VA, USA, 30 March–3 April 2016; pp. 1–6. <https://doi.org/10.1109/SECON.2016.7506667>.
27. Zoha, A.; Gluhak, A.; Nati, M.; Imran, M.A.; Rajasegaran, S. Acoustic and device feature fusion for load recognition. In Proceedings of the 2012 sixth IEEE International Conference Intelligent Systems, Sofia, Bulgaria, 6–8 September 2012; pp. 386–392. <https://doi.org/10.1109/IS.2012.6335166>.
28. Pathak, N.; Al Hafiz Khan, M.A.; Roy, N. Acoustic based appliance state identifications for fine-grained energy analytics. In Proceedings of the 2015 IEEE International Conference on Pervasive Computing and Communications (PerCom), St. Louis, MO, USA, 23–27 March 2015; pp. 63–70. <https://doi.org/10.1109/PERCOM.2015.7146510>.
29. Schneider, M.; Ilgin, S.; Jegenhorst, N.; Kube, R.; Püttjer, S.; Riemschneider, K.R.; Vollmer, J. Automotive battery monitoring by wireless cell sensors. In Proceedings of the 2012 IEEE International Instrumentation and Measurement Technology Conference Proceedings, Graz, Austria, 13–16 May 2012; pp. 816–820.
30. Abd Wahab, M.H.; Anuar, N.I.M.; Ambar, R.; Baharum, A.; Shanta, S.; Sulaiman, M.S.; Hanafi, H. IoT-based battery monitoring system for electric vehicle. *Int. J. Eng. Technol.* **2018**, *7*, 505–510.
31. Thomas, J.K.; Crasta, H.R.; Kausthubha, K.; Gowda, C.; Rao, A. Battery monitoring system using machine learning. *J. Energy Storage* **2021**, *40*, 102741.
32. Li, J.; Wang, L.; Lyu, C.; Liu, E.; Xing, Y.; Pecht, M. A parameter estimation method for a simplified electrochemical model for Li-ion batteries. *Electrochim. Acta* **2018**, *275*, 50–58.
33. Qiu, Y.; Chen, B.; Gu, C. Product development analysis of chargers for electric bicycles. *Electr. Bicycl.* **2016**, *37–38*. (In Chinese)
34. Ma, Y.; Feng, X.; Jiao, J.; Peng, Z.; Qian, S.; Xue, H.; Li, H. Smart fire alarm system with person detection and thermal camera. In Proceedings of the International Conference on Computational Science, Amsterdam, The Netherlands, 3–5 June 2020; Springer: Berlin/Heidelberg, Germany, 2020; pp. 353–366.
35. Zhang, J.; Ji, X.; Chi, Y.; Chen, Y.c.; Wang, B.; Xu, W. OutletSpy: Cross-outlet application inference via power factor correction signal. In Proceedings of the 14th ACM Conference on Security and Privacy in Wireless and Mobile Networks, Abu Dhabi, United Arab Emirates, 28 June–2 July 2021; pp. 181–191.
36. Shao, Z.; Islam, M.A.; Ren, S. Your noise, my signal: Exploiting switching noise for stealthy data exfiltration from desktop computers. In Proceedings of the ACM on Measurement and Analysis of Computing Systems, 2020; Volume 4, pp. 1–39.
37. Guri, M. Power-supplay: Leaking data from air-gapped systems by turning the power-supplies into speakers. *arXiv* **2020**, arXiv:2005.00395.
38. Ji, X.; Zhang, J.; Jiang, S.; Li, J.; Xu, W. CapSpeaker: Injecting Voices to Microphones via Capacitors. In Proceedings of the 2021 ACM SIGSAC Conference on Computer and Communications Security, Virtual Event, 15–19 November 2021; pp. 1915–1929.
39. Yang, Z.; Wang, Y.; Pan, Y.; Huan, R.; Liang, R. Inaudible Sounds from Appliances as Anchors: A New Signal of Opportunity for Indoor Localization. *IEEE Sensors J.* **2022**, *22*, 23267–23276.
40. AltEnergyMag. E-bike Market Size to Expand around USD 120 Billion by 2030. 2022. Available online: <https://www.altenergymag.com/news/2022/09/14/e-bike-market-size-to-expand-around-usd-120-billion-by-2030/38069/> (accessed on).
41. Bhatt, M.; Hurley, W.; Wolfle, W. A new approach to intermittent charging of valve-regulated lead-acid batteries in standby applications. *IEEE Trans. Ind. Electron.* **2005**, *52*, 1337–1342. <https://doi.org/10.1109/TIE.2005.855665>.
42. Ren, D.; Feng, X.; Lu, L.; He, X.; Ouyang, M. Overcharge behaviors and failure mechanism of lithium-ion batteries under different test conditions. *Appl. Energy* **2019**, *250*, 323–332.
43. Texas-Instruments-Incorporated. Power Factor Correction (PFC) Circuit Basics. 2020. Available online: <https://training.ti.com/power-factor-correction-pfc-circuit-basics> (accessed on).
44. MPS. Power Factor Correction (PFC). 2022. Available online: <https://www.monolithicpower.com/en/power-factor-correction> (accessed on).
45. Abidin, M.N.Z. *IEC 61000-3-2 Harmonics Standards Overview*; Schaffner EMC Inc.: Edsion, NJ, USA, 2006.
46. Lee, E.W. Magnetostriction and magnetomechanical effects. *Rep. Prog. Phys.* **1955**, *18*, 184.
47. MathWorks. 2-D Correlation. 2022. Available online: <https://ww2.mathworks.cn/help/vision/ref/2dcorrelation.html> (accessed on).
48. Boll, S. Suppression of acoustic noise in speech using spectral subtraction. *IEEE Trans. Acoust. Speech Signal Process.* **1979**, *27*, 113–120. <https://doi.org/10.1109/TASSP.1979.1163209>.

49. Dragomiretskiy, K.; Zosso, D. Variational mode decomposition. *IEEE Trans. Signal Process.* **2013**, *62*, 531–544.
50. Chen, Y.; Gong, W.; Liu, J.; Cui, Y. I can hear more: Pushing the limit of ultrasound sensing on off-the-shelf mobile devices. In Proceedings of the IEEE INFOCOM 2018-IEEE Conference on Computer Communications, Honolulu, HI, USA, 16–19 April 2018; pp. 2015–2023.

Disclaimer/Publisher’s Note: The statements, opinions and data contained in all publications are solely those of the individual author(s) and contributor(s) and not of MDPI and/or the editor(s). MDPI and/or the editor(s) disclaim responsibility for any injury to people or property resulting from any ideas, methods, instructions or products referred to in the content.